Space Sci Rev (2008) 136: 227–239
DOI 10.1007/s11214-007-9174-6

The IMPACT Solar Wind Electron Analyzer (SWEA)

J.-A. Sauvaud · D. Larson · C. Aoustin · D. Curtis · J.-L. Médale · A. Fedorov · J. Rouzaud · J. Luhmann · T. Moreau · P. Schröder · P. Louarn · I. Dandouras · E. Penou

Received: 21 September 2006 / Accepted: 16 March 2007 /
Published online: 7 June 2007

Abstract SWEA, the solar wind electron analyzers that are part of the IMPACT in situ investigation for the STEREO mission, are described. They are identical on each of the two spacecraft. Both are designed to provide detailed measurements of interplanetary electron distribution functions in the energy range 1∼3000 eV and in a $120° \times 360°$ solid angle sector. This energy range covers the core or thermal solar wind plasma electrons, and the suprathermal halo electrons including the field-aligned heat flux or strahl used to diagnose the interplanetary magnetic field topology. The potential of each analyzer will be varied in order to maintain their energy resolution for spacecraft potentials comparable to the solar wind thermal electron energies. Calibrations have been performed that show the performance of the devices are in good agreement with calculations and will allow precise diagnostics of all of the interplanetary electron populations at the two STEREO spacecraft locations.

Keywords Solar wind · CME · Electrons · Multipoints

1 Introduction

IMPACT (see Luhmann et al., this volume, 2007, for an investigation overview) is one of the STEREO mission's four measurement packages whose principal objective is to understand the origin and consequences of coronal mass ejections (CME's). As one of IMPACT's in situ instruments, the Solar Wind Electron Analyzer, SWEA, measures the distribution function of solar wind core, halo, and strahl electrons from 1 to ∼3000 eV with high spectral and angular resolutions. SWEA is specifically designed to provide accurate measurements even for very cold ($T_{\mathrm{elec}} < 1$ eV) core electrons which provide a tracer of ejected cold prominence

J.-A. Sauvaud (✉) · C. Aoustin · J.-L. Médale · A. Fedorov · J. Rouzaud · P. Louarn · I. Dandouras · E. Penou
CESR, Centre d'Etude Spatiale des Rayonnements, CNRS-UPS, Toulouse, France
e-mail: sauvaud@cesr.fr

D. Larson · D. Curtis · J. Luhmann · T. Moreau · P. Schröder
SSL, Space Science Laboratory, University of California, Berkeley, USA

material in Interplanetary Coronal Mass Ejection (ICME) events. It also provides nearly full sky coverage of the directionality of strahl electrons, for determining the magnetic topology of ICMEs even when the interplanetary magnetic field (IMF) rotates far out of the ecliptic. In order to allow such performances, the potential of SWEA is controlled to compensate for the spacecraft potential. This maintains the full energy resolution of SWEA even for electron energies lower than the spacecraft potential. Distribution functions are obtained with a time resolution between 2 s and 30 s.

2 Scientific Objectives

Electron velocity distribution functions in the solar wind contain three different components: a thermal core and a suprathermal halo, which are typically present at all pitch angles, and a suprathermal magnetic field-aligned "strahl" which is usually directed anti-sunward and which carries the solar wind electron heat flux (Montgomery et al. 1968; Feldman et al. 1975; Rosenbauer et al. 1977; Pilipp et al. 1987). At 1 AU, the core has a typical temperature of 10^5 K and represents about 95% of the total electron number density. The halo population has a typical temperature of 7×10^5 K and represents, together with the strahl, the remaining portion of the total electron number density. Furthermore, above $\sim$2 keV, a nearly isotropic "superhalo" electron component is present even during the quietest times (Lin et al. 1996). This superhalo typically extends to $>$100 keV and its origin is presently unknown. Note that the impulsive acceleration of electrons to $\sim$1 to a few hundred keV is the most common solar particle acceleration process. Whereas Coulomb collisions can largely explain the relative isotropy of the core population, the origin of the halo population, and more specifically the origin of its sunward directed part is still debated. Electrons constantly escaping from the Sun are focused into field aligned strahl by conservation of the magnetic moment and transport heat flux away from the Sun. The halo consists of a background population of suprathermal electrons scattered over very large heliospheric distances. Magnetic focusing acts to narrow the strahl, while scattering processes and the interplanetary potential act to broaden it. Competition between these determines the actual strahl width (Rosenbauer et al. 1977; Gosling et al. 2004). Observations of the strahl in the solar wind is evidence of direct magnetic connection to the Sun. On a heliospheric field line that is disconnected from the Sun, one expects to see the strahl disappear and the electron heat flux to be greatly reduced (e.g., Gosling et al. 2005). However, disconnection is not the only cause of heat flux dropouts. The heat flux often drops at and near the IMF sector boundaries (Pilipp et al. 1990; McComas et al. 1989; Fitzenreiter and Ogilvie 1992; Crooker et al. 2003). However, many of these heat flux dropouts are not apparent in higher-energy electrons, suggesting enhanced scattering over disconnection as the cause in many such events (Lin and Kahler 1992; Fitzenreiter and Ogilvie 1992).

Solar electrons from $\sim$0.1 to 10^2 keV in the energy range covered by SWEA and STE (see Lin et al., this volume, 2007, for a description of the higher energy electron measurements by IMPACT's STE sensor), are thus excellent tracers of the structure and topology of IMF lines since they are fast and have very small gyroradii. An ICME/magnetic cloud often has a force-free configuration and may remain magnetically connected to the Sun even beyond 1 AU (e.g. Larson et al. 1997); its plasma composition and characteristics are often very different from the pre-existing solar wind (e.g. Wurz et al. 1998; Wimmer-Schweingruber et al. 1999). Figure 1 shows plasma and magnetic field data for an ICME event observed near 1 AU. Note the forward shock, the compression of the plasma density and magnetic field, and the slow rotation of the magnetic field vector inside the ICME which in this case was

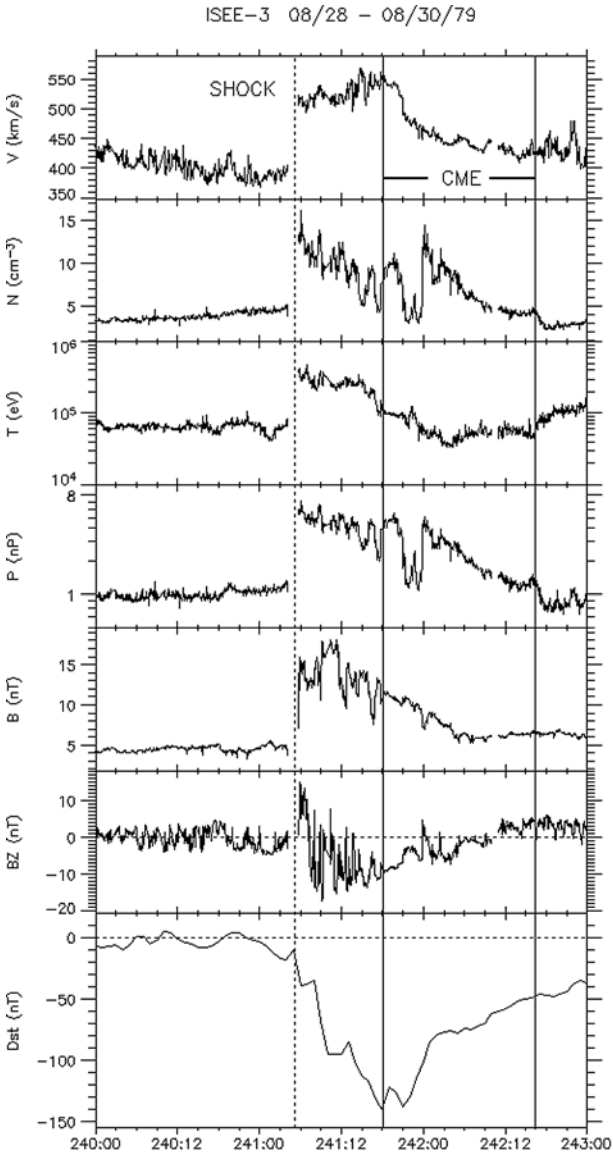

Fig. 1 Plasma and magnetic field data for an ICME event observed near 1 AU and the Dst index. Note the forward shock, the compression of the plasma density and magnetic field, and the slow rotation of the magnetic field vector inside the magnetic cloud (labeled *CME*) itself. Adapted from Gosling and McComas (1987) and Gosling et al. (1990)

a magnetic cloud (e.g., Burlaga 1991). Many questions related to CME/ICME evolution in the solar wind are closely related to the questions of CME origins. For example magnetic clouds often appear to expand as they propagate out through the heliosphere, but the extent of their expansion is likely controlled by the ambient coronal and solar wind conditions as well as their internal structure (e.g. Osherovich and Burlaga 1997; Gosling 1997).

A significant fraction of ICMEs have intervals with very cold electron temperatures T_{ec} (e.g., Montgomery et al. 1974) ranging down to <1 eV, while in non-ICME solar wind, T_{ec} never drops below ∼6 eV. For such an ICME (e.g., the event shown in Fig. 2), detailed fits to electron distributions show that T_{ec} generally range from ∼1 to 4.5 eV (Larson et al. 2000). For most of this ICME the halo density was very low (<0.1 cm^3), suggesting magnetic dis-

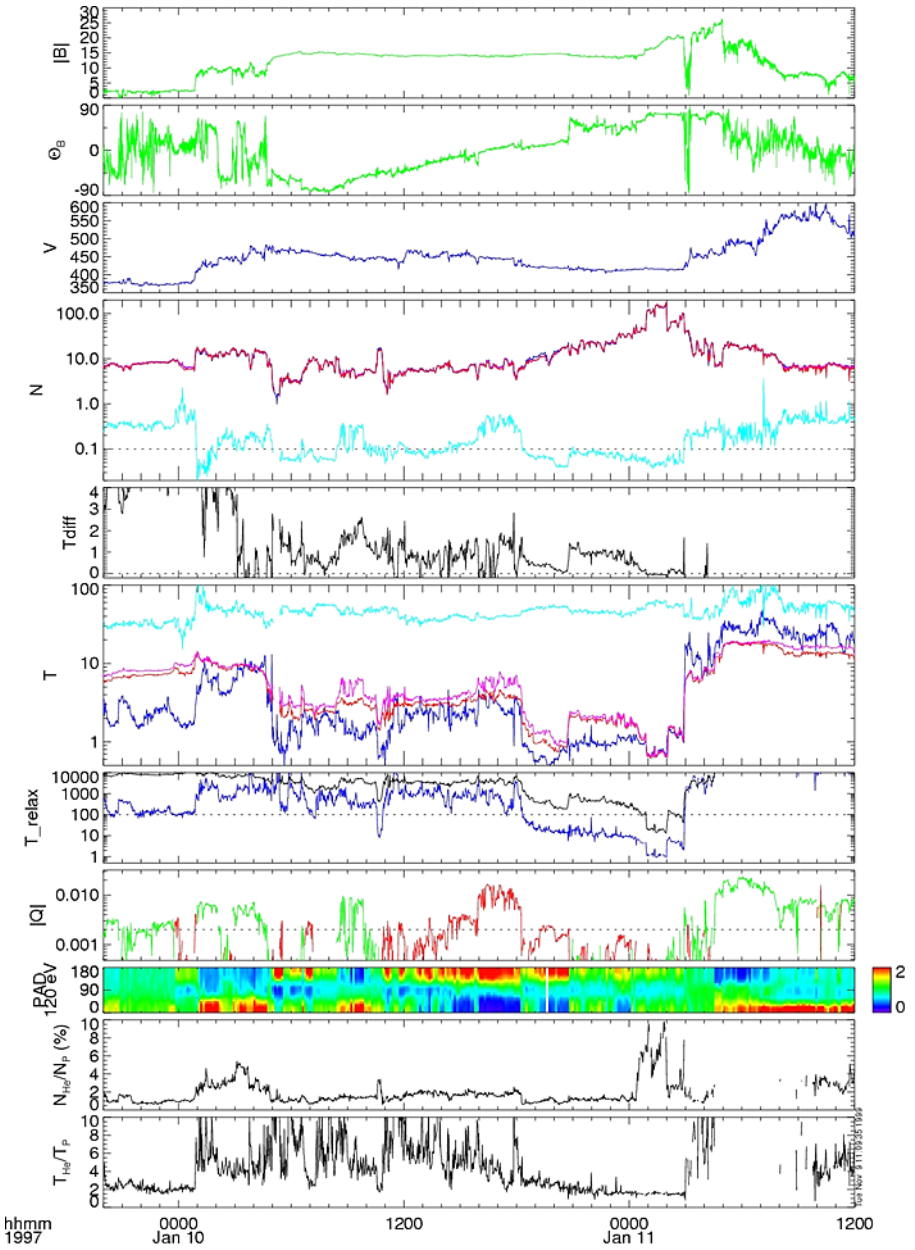

Fig. 2 Summary plot of solar wind parameters: from top to bottom: – 1) magnetic field strength ($|B|$), and – 2) angle out of ecliptic (Θ_B), – 3) plasma bulk speed (V), – 4) density (N) of the electrons (*red*), protons (*blue*) and of the halo electrons (*light blue*), – 5) core electron–proton temperature difference, – 6) temperatures (T) of the protons (*blue*), electrons (*pink*), core electrons (*red*) and halo electrons (*light blue*), – 7), collisional relaxation time (T_{relax}) for electron–proton (*black*) and alpha-proton (*blue*), – 8) electron heat flux parallel to B ($|Q|$), $Q > 0$ in green, – 9) normalized electron flux at 120 eV versus pitch-angle (PAD), – 10) alpha to proton density ratio (N_α/N_p) and – 11) alpha to proton temperature ratio. From Larson et al. 2000

connection from the Sun. Remarkably, during these times the solar wind proton temperature, T_p, is equal to T_{ec}, and shows the same temporal variations. This behavior, which is never observed in the non-ICME solar wind, provides strong evidence that the ICME has evolved through adiabatic cooling as it travel to 1 AU, most likely due to expansion in the radial direction (the solar wind speed decrease through the ICME). In the regions of this ICME where the halo density is at normal levels ($\sim$0.03–0.5 cm^{-3}) T_{ec} increases significantly above T_p, indicating that the core electrons were being heated by the halo. SWEA's precise measurements of very cold core and halo electrons, together with the detailed ion measurements made by the PLASTIC plasma ion composition analyzer on STEREO (see Galvin et al., this volume, 2007), will provide powerful diagnostics of CME/ICME evolution, cooling and heating while the multipoint perspective provided by STEREO measurements and models will illuminate ICME interplanetary evolution and the 3D context of the surrounding solar wind structure.

The magnetosphere of the Earth is driven by the solar wind convection electric field and the solar wind dynamic pressure. While the influence of the first factor is well quantified, the action of the pressure remains less clear and depends on particular situations. Of special importance are large amplitude solar wind pressure enhancements associated with interplanetary shocks and ICMEs. Such pressure jumps significantly move the bow shock and magnetopause earthward, leading to large induced electric fields and to major currents that can couple to the ionosphere and to the ring current and lead to strong ionospheric disturbances. Furthermore, an interplanetary shock can cause large numbers of energetic particles to be injected into the earth's inner magnetosphere, worsening the radiation environment for spacecraft. Heliospheric disturbances are often accompanied by solar energetic particles (SEP) accelerated by interplanetary shocks or solar flares. These high energy particles also interact with the non-magnetized planets Venus and Mars whose upper ionospheric layers are affected by the high solar wind dynamic pressures associated with these heliospheric disturbances. When Venus, Earth and Mars are within the same heliospheric longitudinal sector (e.g. expected in summer 2008), the same ICME may affect all three planets and especially affect their upper atmospheres. Together with the two STEREO spacecraft, the Venus Express (VEX), Mars Global Surveyor (MGS) and Mars Express (MEX) particle and field payloads will be used to track the ICME topology and propagation characteristics in the heliosphere and to assess their effects on the planetary environments.

3 Instrument Overview

The Solar Wind Electron Analyzer – SWEA and the supra-thermal electron detector (STE) are linked together and to the spacecraft command and data handling by the data processing unit. Figure 3 gives the SWEA block diagram and Table 1 summarizes the SWEA measurement parameters and instrument characteristics. Each SWEA consists of an electrostatic analyzer with front-end deflectors to measure electron fluxes from $\sim$1 eV to 3 keV over a solid angle of 360° $\times$ 120° with sufficient sensitivity at the extreme flux levels likely to be encountered. To minimize spacecraft potential effects on the low energy electrons and to provide unimpeded fields-of-view, SWEA and STE are mounted antisunward at the end of the IMPACT boom, 4.5 m from the spacecraft and located in its shadow (Fig. 4). Furthermore in order to keep constant the energy resolution of SWEA, even when solar electrons are accelerated by the spacecraft electrostatic potential, the electrostatic analyzer and the deflectors are biased to a commandable voltage, which is used to decelerate the incoming electrons.

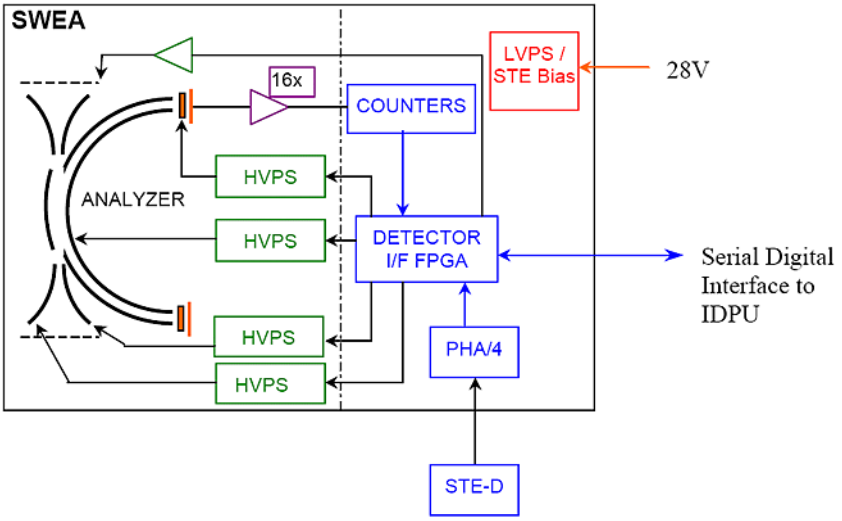

Fig. 3 SWEA block diagram

Table 1 STEREO solar wind electron instrument

A. Measurement parameters

	Electrons energy range	Geometrical factor at 0° elevation ($cm^2 \cdot sr \cdot eV/eV$)	Field of view (°)	Dynamic range $eV/(cm^2 \cdot sr \cdot eV \cdot s)$
SWEA	1 eV–3 keV	8.4×10^{-3}	$360 \times 120°$	$\sim 10^8$

B. Instrument characteristics (without the common SWEA/STE-D pedestal electronics)

	Mass, kg	Power, W	Volume, cm^3	Nominal bit rate, bps
SWEA	0.97	0.55	1150	534

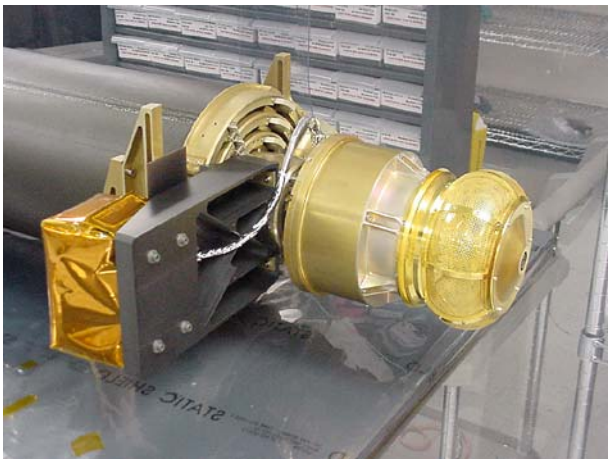

Fig. 4 The solar wind electron analyzer at the end of the stowed IMPACT boom and the magnetometer on its shelf. After boom deployment the two instruments are separated by ~1 m

To fully utilize the capabilities of SWEA and STE, microprocessors are employed to provide physically meaningful on-board data processing and compression, as well as flexible operation. For example, ten moments of the electron distributions: density, the three components of bulk velocity, the six unique elements of the momentum flux tensor and the energy flux vector are computed onboard following every complete energy and angle scan. In addition, the particles can be sorted by pitch angle and reduced distribution functions computed, using the magnetic field vector obtained directly from the on-board magnetometer. Besides the spacecraft power and command and data handling interfaces, the experiment has interfaces to the magnetometer (see the IMPACT Instrument Data Processing Unit (IDPU) discussion in the paper by Luhmann et al., this volume, 2007).

4 Electrostatic Analyzers and Deflectors

The SWEA electrostatic analyzers and deflectors have been designed for measurements of the interplanetary electron core, halo and strahl electrons (1 eV–$\leq$6 keV). The quasi-3D distribution of these particles will be sampled as often as every 2 seconds. The geometrical factor of the analyzer can be electrostatically changed, increasing the range of fluxes that can be measured without detector saturation and allowing direct sampling of the core solar wind electron populations as well as high sensitivity measurements of the suprathermal electrons. The analyzer design is a symmetrical spherical section electrostatic analyzer (Carlson et al. 1983; Carlson and McFadden 1998) with a 360° disk-shaped field of view.

The imaging of parallel rays onto the detector plane provides about 1° inherent analyzer resolution in the detection plane. Ultraviolet light (UV) entering the sensor is a potential background source. The analyzer geometry forces at least a 2 bounce light path to the microchannel plate detector and the smooth inner and scalloped outer hemispheres have a gold black coating applied to further reduce scattered light. Very similar analyzers have been flown on the WIND, Interball and Cluster spacecraft and have provided good solar UV rejection. A grid at the analyzer exit prohibits leakage field from the microchannel plates (MCPs) from entering the analyzer section. Electrons are post-accelerated by a +300 V potential applied to the front of the MCPs to increase detection efficiency to about 70%. An aperture cover, together with a one-time opening mechanism, which maintains an internal dry nitrogen environment during integration and launch, sealed the inside of the analyzer prior to launch.

The SWEA electrostatic analyzer has a 360° planar field-of-view (FOV) that is perpendicular to the ecliptic plane and to the boom carrying SWEA, STE and MAG (Fig. 4). The SWEA FOV is electrostatically deflected into a cone up to $\pm 60°$ out of its normal plane by a voltage applied to curved plates placed at the analyzer entrance aperture (Fig. 3). A pair of grids at the outer analyzer collimator minimizes leakage fields from the deflectors.

The SWEA analyzer has an inner plate radius of 3.75 cm and the plate separation is 0.28 cm. The resulting energy resolution is 17%. The total geometric factor is 0.01 $cm^2 \cdot sr \cdot eV/eV$ including an MCP efficiency of about 70% and grid transmission (3 grids), of 73%. SWEA compensates for the effects of spacecraft potential on the lowest energy particles by having an outer hemisphere that can be biased according to the plasma density measured by the PLASTIC solar wind ion instrument. With V_i and V_0 defined as the potentials of the inner and outer hemispheres, the inter sphere potential drop $\delta V = V_0 - V_i$, the pass band energy and the energy resolution can be written: $\langle E \rangle = qV_0 + k_a q \delta V = q\delta V(\alpha + k_a)$ and $\delta E = w k_a q \delta V$. Here k_a and w are characteristics of the geometry of the top hat and we have defined $\alpha = V_0/\delta V$. For SWEA, $k_a = 10$

and $w \sim 0.17$ (17%). By varying the value of α the relative energy resolution can be varied:

$$\frac{\delta E}{E} = \frac{w}{1 + \alpha/k_a}.$$

Conservation of the phase space volume, $(E\,\mathrm{d}E)\mathrm{d}\Omega\,\mathrm{d}A$, provides the following useful result to compute the geometrical factor corresponding to $V_0 \neq 0$:

$$G_\alpha = \frac{G_0}{1 + \alpha k_a},$$

where G_0 is the geometrical factor of the instrument for $\alpha = 0$. The effective geometrical factor ($\mathrm{cm}^2{\cdot}\mathrm{sr}{\cdot}\mathrm{eV/eV}$) is defined as:

$$g_\alpha = \frac{G_\alpha}{\langle E \rangle} = \frac{g_0}{(1 + \alpha/k_a)^2}.$$

Finally, note that the effect of the retarding potential, V_0, is to improve the energy resolution by a factor $(1 + \alpha/k_a)$ and to lower the geometrical factor by a factor $(1 + \alpha/k_a)^2$. Although the SWEA detector is strictly for electrons, this scheme can be used for ions as well.

SWEA uses MCP detectors in a chevron pair configuration, which gives an electron multiplication gain of about 2×10^6 and a narrow pulse height distribution. The Photonis MCPs are each 1 mm thick. The plates are processed for high strip current to provide fast counting capability. The microchannel plates are on a polyimide printed board that supports the electrostatic analyser and the MCP stack. 16 collectors of 22.5 degrees each are implemented on the MCP side of the board. On the opposite side are a heating circuit and 16 coupling circuits to the amplifier board. A simulation of the magnetic field generated by the current of the heating system was performed and the routing of the power supply line was optimised in order to minimise the impact of that magnetic field on the trajectory of the electrons inside the analyzer.

Charge pulses produced by the MCPs are collected on the set of discrete anodes and sent to preamplifier-discriminators. The amplifiers are A111F amplifiers from Amptek. On the board a pulse generator is implemented to generate test pulses on the input of each amplifier. The threshold of the amplifiers is adjusted at 45pC corresponding to a gain of 2.75×10^5 on the MCP. The maximum count rate of the amplifiers is 2×10^6 pulses per second. The output pulses of the amplifiers are provided to sixteen counters situated on the digital board.

The high voltage board generates four positive high voltages (HV) and one negative voltage to compensate the spacecraft potential (V_0). One HV supplies the MCP. The HV converter can deliver 3.2 kV and it is adjustable by analog command. The three other programmable HVs supply the optics of the instrument, one for the electrostatic analyser with a range from 0 to 750 V and the two others for the two deflectors with a range from 0 to 1500 V. These three positive HVs are delivered by three amplifiers. They are controlled by analog commands generated by the digital board of the instrument. A non-regulated HV converter generates the power supplies of the HV amplifiers. The HVs for the electrostatic analyser and for the deflectors are referenced to the V_0 voltage that can be adjusted in the range from 0 to -25 V. The HV amplifiers have a rise time and fall time of 100 µs and a stability better than 1% in the temperature range from -70°C to $+50$°C. The two HV converters are synchronised at 100 kHz. The SWEA interface provides two digital signals that enable the MCP and the non regulated high voltage supplies. These signals are at zero volts to turn off the supplies and +5 V to turn on the supplies.

5 Calibrations

The calibration of the SWEA sensor has been performed at the CESR Toulouse vacuum facilities and at SSL Berkeley. At CESR, a simple cylindrical electron gun was used as a source of low energy electrons (~600 eV). The mechanical setup of the electron gun and of the sensor is shown in Fig. 5. The electron beam current was monitored and stabilized using the total current on the cylinder surrounding the gun. The gun produces a rather narrow beam, so that uniform illumination of the SWEA effective aperture was obtained by scanning the gun in the vertical and horizontal directions. The sensor was mounted on the turntable table allowing azimuthal and elevation angles of the electron beam to be set with an accuracy of 0.1°.

The MCP dead-time was measured by illuminating the MCP surface via small pin-holes with electron fluxes of different intensities. Knowing the beam current in each case, and measuring the non-linear profile of the MCP count rate as a function of the beam current, allowed us to determine the dead-time of one micro channel to be 200 ms.

The Energy (eV)/Voltage (V) ratio of the analyzer, k, was found to be nearly independent of the voltage applied to the deflectors and equal to 6.28 for sector "1". But there is a non-negligible variation of k with azimuth due to the non-concentric inner and outer hemispheres. Figure 6 shows this variation that can be described by:

$$k = 6.26 + 1.17 \cdot 10^{-2} \sin(\phi - 65.1) + 6.8 \cdot 10^{-2} \cos(\phi - 65.1).$$

Here $\phi = 0$ corresponds to the center of sector "1".

The energy resolution of the analyzer was found to be almost constant for all values of the elevation and azimuth and equal to 0.167. The total geometrical factor G of each of the 16 anodes for a zero elevation angle are given in Table 1. G is in 10^{-4} cm^2·sr·eV/eV.

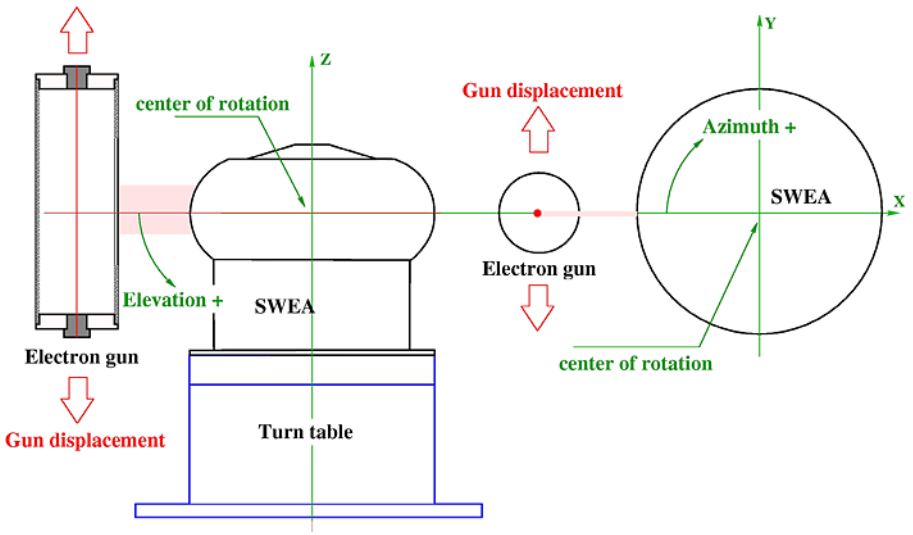

Fig. 5 Mechanical setup of the electron gun and sensor for calibrations

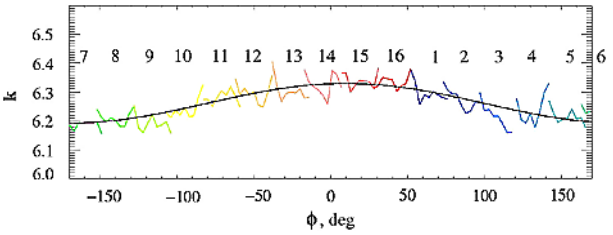

Fig. 6 Variation of the energy/voltage ratio of the analyzer, k, as a function of azimuth for zero degrees elevation. *Colors* and *numbers* refer to different sensor sectors

Table 2 Geometrical factors of the 16 anodes for a zero degree elevation

A	1	2	3	4	5	6	7	8	9	10	11	12	13	14	15	16
G	4.8	5.8	5.7	5.2	5.6	6.2	4.3	4.4	5.3	5.8	5.6	4.9	5.3	5.2	5.0	4.8

The energy-angular response of the analyzer depends on the deflection angle of the electrons, defined by the following parameter:

$$D = \frac{U_{\text{defTHV}} - U_{\text{defBHV}}}{E} = \frac{U_{\text{def}}}{E}.$$

Here U_{defTHV} and U_{defBHV} are voltages of the top and bottom electrodes of the deflector.

The variation of the energy-angular response of the analyzer is illustrated in Fig. 7, which shows examples for several values of D compared with simulation results. The top row of panels correspond to $D = -0.59$, the middle row corresponds to $D = 0.03$, and the bottom row corresponds to $D = 0.71$. The measurements of the central elevation angle, θ, as a function of the D-factor gives an excellent, almost linear, relation between θ and D:

$$\theta = -2.9 + 78.3 \times D - 1.22 \times D^2.$$

The geometrical factor of the sensor depends on the elevation angle. Figure 8 shows the variation of the $\mathrm{d}G/\mathrm{d}\phi$ value corresponding to the center of sector "1" as a function of θ. To obtain the total geometrical factor of the sector this value must be integrated over ϕ. Accurate measurements can be done between -50 and $+50$ degrees of elevation angle (Fig. 8). Beyond these extremes the geometrical factor of the sensor (as well as other parameters) degrades quickly.

6 Digital Electronics

SWEA/STE-D share a common set of digital electronics and a low voltage power supply. Most of the digital electronics is contained in an Actel FPGA, supplemented by Digital to Analog converters to generate control voltages and an Analog to Digital converter to provide housekeeping measurements. The digital electronics includes 16 counters for the preamp-discriminators that are read out to the IMPACT Instrument Data Processing Unit, IDPU, every high voltage step (5.8 ms). The digital electronics also control the analyzer high voltage supplies and V_0 supply from a look-up table loaded by the IDPU. The look-up table contains a full sweep profile for the two deflector supplies, the analyzer supply, and V_0. The MCP supply is programmed to a fixed value provided by the IDPU. The nominal profile consists of an exponentially decaying analyzer voltage with a 2-second period. The deflector

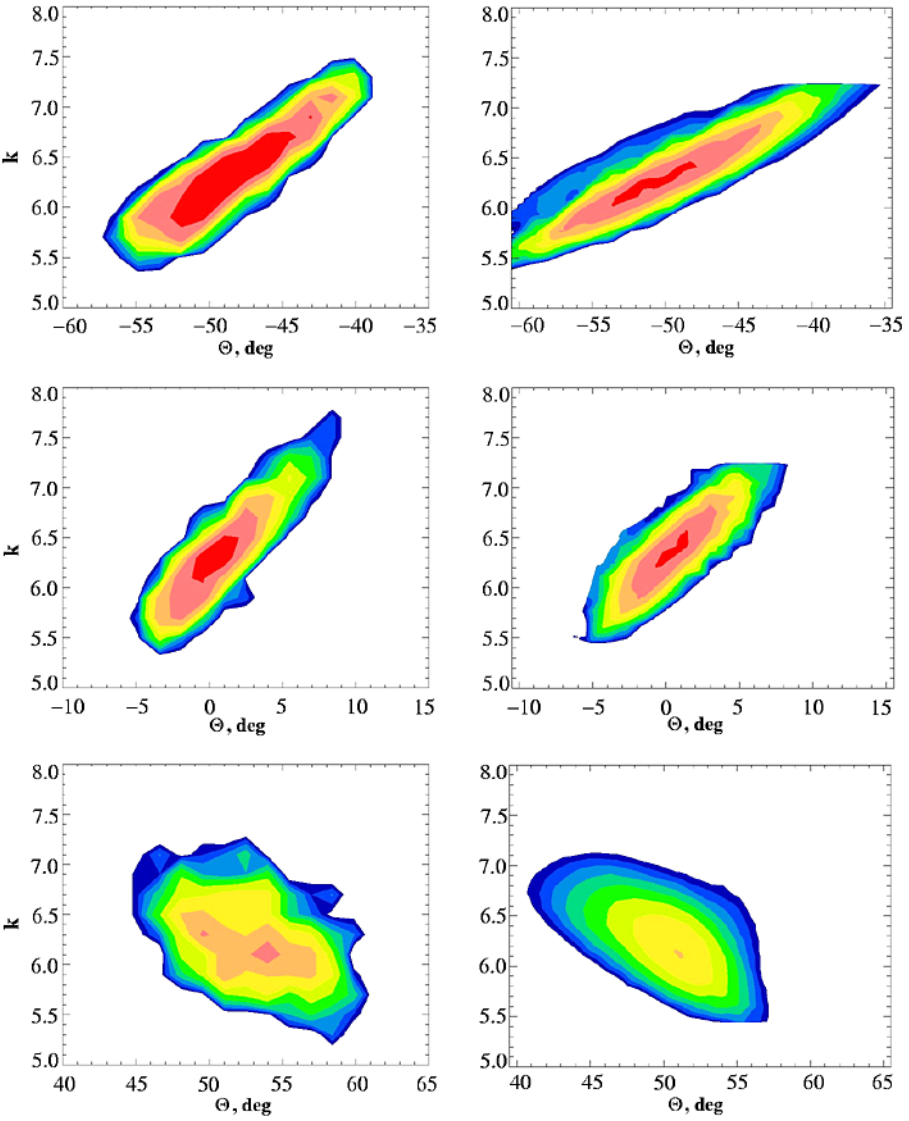

Fig. 7 Energy-angular responses of SWEA. The *left column* corresponds to the measurements, and the *right column* corresponds to numerical simulations. The *top*, *middle* and *bottom rows* correspond to different deflection angles of the electrons (see text)

supplies ramp up and down 48 times during the sweep to a maximum voltage proportional to the analyzer voltage in order to sample the full range of deflection angles. The counter readout is synchronized to the sweep waveform in order to provide 6 deflection samples (at ∼22 degree resolution) for each of 48 energy steps. The digital electronics also controls the SWEA operational heater, the SWEA aperture door actuator, and the SWEA test pulser, in addition to STE-D functions. A high voltage enable plug mounted to the digital electronics

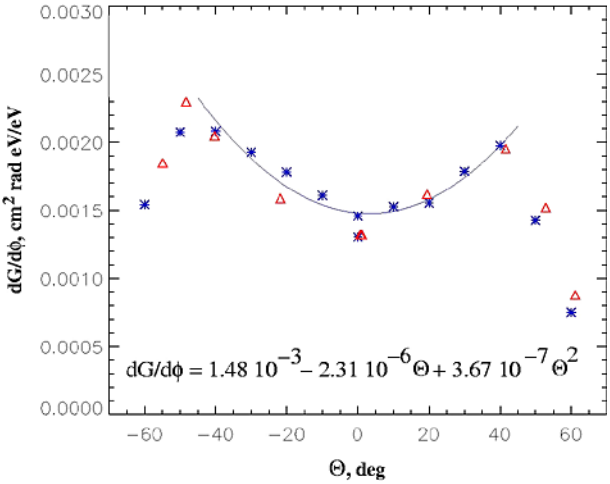

Fig. 8 $dG/d\phi$ measured at the center of sector "1" versus the elevation angle

interrupts primary power to the high voltage supplies to render the instrument safe on the ground.

7 Experiment Modes of Operations

SWEA has a single mode of operation, adjusted by a large number of programmable parameters such as MCP voltage and analyzer sweep supply waveform generation parameters. The nominal operational mode causes the instrument to sweep over the full range of deflections and energies every 2 seconds as described in Sect. 6. The data are read out and collected into a matrix corresponding to the measured electron distribution function. These data are sent with full time resolution to the burst memory, and are sampled every 30 seconds for normal (continuous) telemetry. Moments of the distribution function with full time resolution are computed and sent every 2 seconds. A pitch angle distribution is also extracted based on the measured magnetic field direction and sent every 10 seconds. All this processing takes place in the IDPU.

8 Summary

The Solar Wind Electron Analyzers, SWEAs, onboard STEREO are designed to provide precise measurements of the low energy electrons in interplanetary space at 1 AU over a wide range of energies, angles and fluxes. Because of the large amount of data generated by SWEA, substantial data selection and compression are performed. On a routine basis, these instruments provide measurements of the solar wind electron density, temperatures, pitch-angle distributions, heat flux and velocity. The variable potential of the instruments allows valuable measurements to be obtained even when the positive potential of the satellites is of the order of the measured electron energy.

Acknowledgements The realization of the SWEA sensor heads and of their calibrations has been supported by CNES under Contract No. CNES-221. We thank E. Le Comte for his support in the calibration process.

References

L.F. Burlaga, in *Physics of the Inner Heliosphere, 2.*, ed. by R. Schwenn, E. Marsch (Springer, Berlin, 1991), pp. 1–22

C.W. Carlson, J.P. McFadden, in *Measurements Techniques in Space Plasmas: Particles*, ed. by R.F. Pfaff, J.E. Borovsky, D.S. Young (AGU, Washington, 1998), pp. 125–140

C.W. Carlson, D.W. Curtis, G. Poschmann, W. Michael, Adv. Space Res. **2**, 67 (1983)

N.U. Crooker, D.E. Larson, S.W. Kahler, S.M. Lamassa, H.E. Spence, Geophys. Res. Lett. **30**(12), 1619 (2003). doi:10.1029/2003GL017036

W.C. Feldman, J.R. Asbridge, S.J. Bame, M.D. Montgomery, S.P. Gary, J. Geophys. Res. **80**, 4181–4196 (1975)

R.J. Fitzenreiter, K.W. Ogilvie, J. Geophys. Res. **97**, 19,213–19,219 (1992)

Galvin et al. (2007, this volume)

J.T. Gosling, D.J. McComas, Geophys. Res. Lett. **14**, 355 (1987)

J.T. Gosling, S.J. Bame, D.J. McComas, J.L. Phillips, Geophys. Res. Lett. **17**, 901 (1990)

J.T. Gosling, in *Coronal Mass Ejections*, ed. by N.U. Crooker, J.A. Jocelyn, J. Feyman. American Geophys. Union Monog., vol. 99 (American Geophys. Union, 1997), p. 9

J.T. Gosling, C.A. de Koning, R.M. Skoug, J.T. Steinberg, D.J. McComas, J. Geophys. Res. **109**, A05102 (2004). doi:10.1029/2003JA010338

J.T. Gosling, R.M. Skoug, D.J. McComas, C.W. Smith, Geophys. Res. Lett. **32**, L05105 (2005)

D.E. Larson et al., Geophys. Res. Lett. **24**, 1911 (1997)

D.E. Larson, R.P. Lin, L. Steinberg, Geophys. Res. Lett. **27**(2), 157 (2000)

R.P. Lin, S.W. Kahler, J. Geophys. Res. **97**(A6), 8203–8209 (1992)

R.P. Lin, D. Larson, J. McFadden, C.W. Carlson, R.E. Ergun, K.A. Anderson, S. Ashford, M. McCarthy, G.K. Parks, H. Reme, J.M. Bosqued, C. d'Uston, T.R. Sanderson, K.-P. Wenzel, Geophys. Res. Lett. **23**(10), 1211–1214 (1996)

R.P. Lin et al. (2007, this volume)

J.G. Luhmann, D.W. Curtis, P. Schroeder, J. McCauley, R.P. Lin, D.E. Larson et al., Space Sci. Rev. (2007, this volume), doi:10.1007/s11214-007-9170-x

D.J. McComas, J.T. Gosling, J.L. Phillips, S.J. Bame, J. Geophys. Res. **94**, 6907–6916 (1989)

M.D. Montgomery, S.J. Bame, A.J. Hundhausen, J. Geophys. Res. **73**, 4999–5003 (1968)

M.D. Montgomery, J.R. Asbridge, S.J. Bame, W.C. Feldman, J. Geophys. Res. **79**, 3103 (1974)

V. Osherovich, L.F. Burlaga, in *Coronal Mass Ejections*, ed. by N.U. Crooker, J.A. Jocelyn, J. Feyman. American Geophys. Monog., vol. 99 (American Geophys. Union, 1997), p. 9

W.G. Pilipp, H. Miggenrieder, M.D. Montgomery, K.-H. Muhlhauser, H. Rosenbauer, R. Schwenn, J. Geophys. Res. **92**, 1075 (1987)

W.G. Pilipp, H. Miggenieder, K.-H. Mühläuser, H. Rosenbauer, R. Schwenn, J. Geophys. Res. **95**, 6305–6329 (1990)

H. Rosenbauer, R. Schwenn, E. Marsch, B. Meyer, H. Miggenrieder, M.D. Montgomery, K.H. Muehlaeuser, W. Pilipp, W. Voges, S.M. Zink, J. Geophys. **42**, 561 (1977)

R.F. Wimmer-Schweingruber, O. Kern, D.C. Hamilton, Geophys. Res. Lett. **26**, 3541 (1999)

P. Wurz et al., Geophys. Res. Lett. **25**, 2557 (1998)